Vadillo, D.C., Tembely, M., Morrison, N.F., Harlen, O.G., Mackley, M.R. and Soucemarianadin, A., Submitted to Journal of Rheology, 'The matching of polymer solution fast filament stretching, relaxation and break up experimental results with 1D and 2D numerical viscoeastic simulation'. (2012). Accepted.

1

2

3

4

The matching of polymer solution fast filament stretching, relaxation and

break up experimental results with 1D and 2D numerical viscoelastic

simulation.

by

D. C. Vadillo[*1], M. Tembely[**2], N.F. Morrison[3], O. G. Harlen[3], M. R. Mackley[1]

and A. Soucemarianadin[***2]

[1]Department of Chemical Engineering and Biotechnology, University of Cambridge,

CB2 3RA, UK

[2]Laboratory for Geophysical and Industrial Flow (LEGI, UMR 5519)

University Joseph Fourier, Grenoble, BP 53, 38041 Grenoble Cedex, France

[3] School of Mathematics, University of Leeds, Leeds. LS2 9JT, UK

[*] DV current address. AkzoNobel Research, Development and Innovation, Stoneygate

Lane, Felling, Gateshead, NE10 0JY, UK

20   ** MT current address: Concordia University, Department of Mechanical and

21   Industrial Engineering, Montréal (Québec) H3G 1M8, Canada

22   *** AS presently in delegation at Campus France, Paris, France

23

24

25   **Abstract**

26   This paper is concerned with the comparison of two numerical viscoelastic strategies

27   for predicting the fast filament stretching, relaxation and break up of low viscosity,

28   weakly elastic polymeric fluids. Experimental data on stretch, relaxation and breakup

29   was obtained using a Cambridge Trimaster for a Newtonian solvent (DEP) and three

30   monodisperse polystyrene polymer solutions. Two numerical codes were tested to

31   simulate the flow numerically. One code used a 1D approximation coupled with the

32   Arbitrary Lagrangian Eulerian (ALE) approach and the other a 2D axisymmetric

33   approximation for the flow. In both cases the same constitutive equations and mono

34   and multimode parameter fitting was used; thereby enabling a direct comparison on

35   both codes and their respective fit to the experimental data. Both simulations fitted the

36   experimental data well and surprisingly the 1D code closely matched that of the 2D.

37   In both cases it was found necessary to utilise a multimode approach to obtain a

38   realistic match to the experimental data. The sensitivity of the simulation to the choice

39   of constitutive equation (Oldroyd-B and FENE-CR) and the magnitude of non linear

40   parameters were also investigated. The results are of particular relevance to ink jet

41   processing and demonstrate that high shear rate, low viscosity viscoelastic polymeric

42   flows can be simulated with reasonable accuracy.

43   **1.Introduction**

44   The way in which viscoelastic fluids stretch, thin and break up is of relevance to a

45   number of technologies and these three phases of the flow have in the past received

46   extensive scientific attention; although generally as three different individual topics.

47   The stretching of polymeric fluids in particular has received detailed experimental and

48   modeling attention in the last decade from amongst others (Anna and McKinley

49   (2001), McKinley and Sridhar (2002), Bach et al. (2002), Clasen et al. (2006)) where

50   the work has concentrated on determining the transient extensional viscosity of fluids.

51   The thinning of prestretched polymeric fluids has also been investigated

52   experimentally following pioneering experimental work by (Bazilevsky et al., 1997)

53   which was subsequently modelled by (Entov and Hinch (1997)). A review by

54   McKinley (2005a) gives an authoritative account of factors that influence filament

55   thinning behaviour. Filament breakup is a delicate process and is the least well

56   characterized and modelled of the three topics amongst stretching, relaxation and

57   breakup covered by this paper.

58   Ink jet printing can involve all three elements mentioned above during filament

59   formation and droplet breakup (Dong et al. (2006), Hoath et al. (2009), Jang et al.

60   (2009)). Although filament thinning experiment cannot reach filament stretching

61   strain rate anywhere near inkjet printing processing, it enables measuring very short

62   extensional relaxation time with timescale comparable with inkjet droplet formation

63   (Vadillo et al., 2012). It also gives access to the elasto-capillary times controlling

64   filament behavior and break-up process (Tembely et al. 2011). As such, filament

65   thinning simulations is therefore a way to test different constitutive equations with

66   well controlled boundary conditions which may eventually lead to a better

67   understanding of the inkjet process which is much more challenging by itself. In

68   order to mimic elements of this complex deformation process a "Cambridge

69   Trimaster" geometry apparatus was developed specifically as a device to capture

70   aspects of the process with well-defined boundary conditions (Vadillo et al. (2010a)).

71   The Cambridge Trimaster has strong similarity to the single piston Rozhkov filament

72   thinning device (Bazilevsky et al. (1990) and the Haake Caber filament thinning

73   apparatus   (http://www.thermo.com/com/cda/product/detail/).   The   twin   piston

74   Trimaster was developed specifically for low viscosity fluids with a fast, controlled

75   initial displacement and for use with high speed photography [Vadillo et al.(2010a)].

76   Characterisation of low viscosity, linear viscoelasticity with short relaxation times is a

77   challenging area of rheology, however the Pechold, Piezo Axial Vibrator (PAV)

78   (Groß et al. (2002), Kirschenmann (2003), Crassous et al. (2005), and Vadillo et al.

79   (2010b)) is an apparatus that can probe fluid within the range of millisecond

80   relaxation times. Thus by using a combination of the Cambridge Trimaster and the

81   PAV it was possible to probe both the extensional filament break up behaviour of

82   viscoelastic fluids that are well characterized, at least in the Linear Viscoelastic

83   (LVE) regime using the PAV.

84   In a recent work, some authors of this paper have published the matching of

85   experimental and simulation filament stretching and thinning data using the single

86   mode Maxwell description for the viscoelastic contribution of the fluid (Tembely et

87   al. (2012). The results were promising, although all the elements of the Trimaster data

88   with a single mode 1D simulation of the process of thinning and break up could not be

89   fully captured. A direct comparison between 1D and 2D models may be found in the

90   work of Yildirim and Basaran (2001) and more recently by Furlani and Hanchak

91   (2011). The latter authors have used the slender jet 1D approximation and solved the

92   arising nonlinear partial differential equations using the method-of lines wherein the

93   PDEs are transformed to a system of ordinary differential equations for the nodal

94   values of the jet variables on a uniform staggered grid. The results are impressive with

95   the key advantages being the ease of implementation and the speed of computation

96   albeit in a different configuration than the problem considered in this paper. In the

97   present paper, Trimaster data for polymer solutions are matched to single and

98   multimode viscoelastic simulation data, using both a computationally time efficient

5

99   1D simulation and a potentially more rigorous 2D simulation. The paper represents a

100   "state of art" position in matching extensional time dependent results with high level

101   numerical simulation, thereby enabling the effects of constitutive equation and

102   constitutive parameters to be tested.

103   **2.Test fluids, rheological characterisation and Trimaster experimental protocols.**

104   **2a Test fluid preparation and characterisation.**

105   The fluids used were a series of mono-disperse polystyrene dissolved in diethyl

106   phthalate (DEP) solvent as previously described in [Vadillo et al., 2010]. Near mono

107   disperse Polystyrene polymer was manufactured specially by Dow, and gel

108   permeation chromatography (GPC) with THF as the solvent enabled determination of

109   mass and number average molecular weights M_w and M_n as 110 kg/mol and

110   105kg/mol respectively. A stock solution of PS dilution series was prepared by adding

111   10wt% of PS to the DEP at ambient temperature. The resulting solution was heated to

112   180°C and stirred for several hours until the polymer was fully dissolved. The

113   dilution series were prepared by subsequent dilution of the respective stock solutions.

114   Sample surface tension remained constant at 37mN/m up to 10wt% PS110

115   concentration and with a critical polymer overlap concentration c* of 2.40wt%

116   [Clasen et al. (2006a)]. The zero shear viscosities η_0 of the solutions were determined

117   from PAV low frequency complex viscosity η^* data within the terminal relaxation

118   regime and the measured viscosities are given in Table I.

119   **Table I:** Zero shear rate complex viscosity of the different polymer solutions at 25°C

120   **2b. Rheological characterisation.**

6

121   The Piezo Axial Vibrator (PAV) has been used to characterise the linear viscoelastic

122   behaviour of samples with viscosity has low as 1mPa.s on a frequency range

123   comprised between 0.1Hz and 10000Hz [Groß et al. (2002); Kirschenmann (2003);

124   Crassous et al. (2005); Vadillo et al. (2010b   The PAV measures the complex

125   modulus G^* of the test fluid with $G^* = G' + iG''$ and where G' is the storage modulus

126   and G'' is the loss modulus. The complex viscosity η^* is related to the complex

127   modulus by $\eta^* = G^*/\omega$ where ω is the angular frequency. Experimental LVE results

128   are presented in Fig. 1. Loss modulus G'' and elastic modulus G' have been found to

129   increase with the frequency and to vertically shift with the polymer addition. Note, the

130   pure DEP solvent does not show any G'. Both moduli approach at lower frequencies

131   the terminal relaxation regime with the expected scaling with a power of 1 for the loss

132   modulus (Fig. 1.a), and a power of 2 for the storage modulus (Fig. 1.b), and a constant

133   complex viscosity η^* in this regime as shown in Fig. 1.c (except for 5wt% PS110 after

134   2000Hz). The experimental results are displayed between 10^2 and 10^4Hz, the range

135   on which the storage modulus has been captured. At lower frequency, the fluids have

136   been found essentially to behave as a Newtonian fluid with the presence of a loss

137   modulus only.

138   **2c. Cambridge Trimaster experimental protocol**

139   The Cambridge Trimaster (CTM) is a Capillary Breakup Extensional Rheometer that

140   has been specifically designed to probe the extensional rheology of weakly

141   viscoelastic fluids. This apparatus performs a fast stretch of a cylinder of fluid

142   initially located between two identical pistons over a short distance. This apparatus

143   and its limitation have been presented in details in [Vadillo et al. 2010a]. In the

144   present study, the piston diameters are 1.2mm and the experimental filament

145   stretching conditions are an initial gap size L_0 of 0.6mm and a stretching distance L_f

146   of 0.8mm at a relative piston speed $2V_p$ of 150mm/s. This corresponds to a filament

147   strain rate $2V_p/L_0 = 250$ s^{-1} and a filament aspect ratio L_f/L_0 of 2.3. The piston

148   velocity and stretching distance have been chosen to ensure that pistons stop their

149   motions before the critical time scale for inertio-capillary break up for the sample

150   with the lower viscosity, here the DEP. For such a fluid, this time scale has been

151   estimated around 5ms [Tembely et al., 2012].   These conditions will be conserved in

152   the following for both experiments and simulations.

153   The transient filament profiles have been captured using a Photron Fastcam

154   (http://www.photron.com/index.php?cmd=product_general&product_id=1) 1024 PCI

155   high speed camera at 6000 fps, for a picture size of 128 x 256 with a shutter time of

156   3µs. The filament thinning measurement, as well as the filament breakup behaviour,

157   was obtained using automatic image processing based of greyscale variation

158   throughout image for edge detection and the minimum diameter that can be resolved

159   was about 6µm.

160   **2d Relaxation time and moduli determination.**

161   Relaxation spectrum determination from LVE measurements is an ill-posed problem

162   and has been studied extensively in the literature [see for example Baumgaertel and

163   Winter (1989); Kamath et al. (1990), Stadler and Bailly (2009)] and different

164   techniques from linear to non-linear regression have been developed to obtain

165   relaxation spectra from oscillatory LVE data. In the modelling carried out here, a

166   series of equidistant relaxation times spaced on the logarithmic scale was chosen with

167   one mode per decade. This was motivated by the fact that, in experiments, low visco-

168   elastic fluids have shown significant differences between relaxation times in shear and

169 in extension [Clasen et al. (2006)] and recent simulations have shown that using a

170 single mode Maxwell description of the fluid was not sufficient [Tembely et al.

171 (2012)] to capture those differences. The minimization program for both G' and G''

172 data was solved using Matlab®. The solution involved the use of SQP (Sequential

173 quadratic programming) [Jorge and Wright (2006)] methods which may be considered

174 as a state of the art nonlinear programming optimization technique. This method has

175 been shown to outperform other methods in terms of accuracy, efficiency, and

176 adaptability over a large number of problems [Schittkowski (1985)] and it is an

177 effective method for non-linear optimization with constraints. In each iteration the

178 non-linear problem was approximated using a quadratic which is easy to solve (hence

179 the name SQP).

180 The conversion of the experimental data (G'$_m$, G''$_m$, ω_j) into a relaxation function was

181 performed by expressing G(t) as a discrete relaxation spectrum (g_i, λ_i). The Maxwell

182 model relates the real and imaginary parts of the complex modulus determined in

183 LVE measurement to the discrete relaxation spectrum of N relaxation times λ_i and a

184 relaxation strengths g_i through:

185
$$G'(\omega) = \sum_{i=1}^{N} g_i \frac{(\omega\lambda_i)^2}{1+(\omega\lambda_i)^2} \qquad (1)$$

186
$$G''(\omega) = \eta_s\omega + \sum_{i=1}^{N} g_i \frac{\omega\lambda_i}{1+(\omega\lambda_i)^2} \qquad (1)$$

187 with ω being the angular frequency of the experiment, and N is the number of

188 relaxation modes. As indicated in (2), G'' accounts for the solvent viscosity.

189 Generally the spectra can be computed by minimizing the "least mean square error"

190 as follows [Bird et al. (1987); Stadler and Bailly (2009)]:

191
$$D = \sum_{j=1}^{M} \left[\frac{G'(\omega_j)}{G'_m(\omega_j)} - 1 \right]^2 + \left[\frac{G''(\omega_j)}{G''_m(\omega_j)} - 1 \right]^2$$
(2)

192 where M is the number of measurements.

193 The model is initialized by choosing the relaxation times to be equidistantly spaced on

194 a logarithmic scale such that $\log(\lambda_i / \lambda_{i+1}) = 1/p$. Setting p = 1, i.e, one mode per

195 decade, has been found to provide sufficient accuracy to accurately describe the LVE

196 behavior (Fig. 1). In the numerical simulation, the Maxwell component of the model

197 was fitted with 5 modes. The relaxation times are chosen such that G' and G''

198 measured over the frequency range $\omega_{min} < \omega < \omega_{max}$ recover all the information

199 regarding the relaxation spectrum over the range $1/\omega_{max} < \lambda_i < 1/\omega_{min}$, however the

200 correct range is given by $e^{\pi/2}/\omega_{max} < \lambda_i < e^{-\pi/2}/\omega_{min}$ [Davies and Anderssen (1997)].

201 This spectrum is a generalized form of the Maxwellian dynamics [Ferry (1980)] and

202 shown in Table II.

203 **3**. **General equations and numerical simulations.**

204 Numerical simulations of the Trimaster deformation were performed using both a

205 one-dimensional model and a 2D axisymmetric model. In the following sub-sections

206 the general equations and the numerical techniques used in both cases are detailed.

207 **3a. Flow geometry.**

208 To model the experimental conditions, an initial cylindrical column of fluid was

209 considered bounded by two rigid circular pistons of diameter D_0. The fluid and the

210 pistons were initially at rest; subsequently the pistons moved vertically outwards with

211 time-dependent velocities $V_p(t)$ (top piston) and $-V_p(t)$ (bottom piston), which are

212 prescribed functions based on fitting a smooth tanh curves through measurements of

213 the Trimaster piston motion in the experiments. As described in Tembely et al 2011,

214 the form of tanh has been chosen to fit the symmetrical "S" shape experimentally

215 observed for the piston motion with time. In they work, the authors have shown that

216 the use of an accurate representation of the piston dynamic response is of importance

217 in the simulation of fast transient dynamic of low viscosity and/or low viscoelasticity

218 fluids.

219 Using a cylindrical coordinate system {r, θ, z}, the flow was constrained to be

220 axisymmetric so that all flow fields are independent of the angular coordinate θ, and

221 the simulation may be restricted to the rz-plane. The coordinate origin is at the axis of

222 the jet, midway between the initial positions of the two pistons. Fig. 2 shows a

223 schematic diagram of the computational domain at an intermediate stage of the piston

224 motion.

225 Symmetric boundary conditions are required along the z-axis to maintain

226 axisymmetry, and conditions of no-slip were applied at each piston surface. The

227 boundary conditions at the free surface are those of zero shear stress and the

228 interfacial pressure discontinuity due to the surface curvature

229 $$\mathbf{t}.\underline{\underline{\mathbf{T}}}.\mathbf{n} = 0 \quad \text{and} \quad \left[\underline{\underline{\mathbf{T}}}.\mathbf{n}\right]_{\text{air}}^{\text{fluid}} = -\gamma\kappa \ , \tag{3}$$

230 where $\underline{\underline{\mathbf{T}}}$ is the total stress tensor, $\mathbf{n}$ is the unit vector normal to the free surface

231 (directed outward from the fluid), $\mathbf{t}$ is the unit tangent vector to the free surface in the

232 rz-plane, γ is the coefficient of surface tension, and κ is the curvature of the interface.

233 It is assumed that the external air pressure is a negligible constant.

234 The location of the free surface at each time-step was determined implicitly via a

235 kinematic condition.   In the axisymmetric simulations, this was realized

236 automatically, since the mesh is Lagrangian and the mesh nodes are advected with the

237 local fluid velocity. The contact lines between the free surface and the pistons were

238 held pinned at the piston edges throughout.

239 The initial conditions are that the fluid is at rest ($\mathbf{v}=\mathbf{0}$) and the polymer is at

240 unstretched equilibrium ($\mathbf{A}_i=\mathbf{I}$).

3b. Governing equations

242 The governing equations for incompressible isothermal flow of a viscoelastic fluid are

243 the classical Navier-Stokes equations for Newtonian fluids together with an additional

244 viscoelastic term coming from the extra stress tensor $\underline{\underline{\sigma}}$. The momentum conservation

245 then may be expressed as follows in which the 3rd term on right-hand-side accounts

246 for viscoelasticity:

$$\rho \frac{d\mathbf{v}}{dt} + \rho(\mathbf{v}.\nabla)\mathbf{v} = -\nabla p + \eta_s \nabla^2 \mathbf{v} + \nabla.\underline{\underline{\sigma}} + \rho g\mathbf{z} \tag{4}$$

248 and the continuity equation reads:

$$\nabla.\mathbf{v} = 0 \tag{5}$$

250 where p is the fluid pressure, ρ is the fluid density, η_s is the solvent viscosity, and g is

251 the acceleration due to gravity.

3c. Constitutive equations

253 For the viscoelastic fluid models, the polymer contribution was described by a

254 Finitely Extensible Nonlinear Elastic (FENE) dumbbell model which makes use of

255 the conformation tensor $\mathbf{A}$, and the stress tensor reads [see for example, Chilcott and

256 Rallison (1988)]:

257
$$\boldsymbol{\sigma} = Gf(R)(\mathbf{A} - \mathbf{I}) \tag{6}$$

258 where G is the elastic modulus, $f(R)$ is the finite extensibility factor related to the

259 finite extensibility parameter L, representing the ratio of a fully extended polymer

260 (dumbbell) to its equilibrium length and R = Tr(A). L can be described in terms of

261 molecular parameters as:

262
$$L = \sqrt{3}\left[\frac{j\left(\sin\frac{\theta}{2}\right)^2 M_w}{C_\infty M_u}\right]^{1-\nu} \tag{7}$$

263 In this expression, θ corresponds to the C-C bond angle and is equal to 109.5°, j

264 corresponds to the number of bonds (2 in the case of PS) of a monomer of molar mass

265 M_u = 104g/mol, C_∞ is the characteristic ratio for a given polymer equal to 9.6, M_w is

266 the molecular weight of the polymer and ν is the excluded volume exponent equals to

267 0.57 for PS110 [Clasen et al. (2006b)]. In the case where the dumbbells are infinitely

268 extensible, $f(R) = 1$ and the constitutive equation is that of an Oldroyd-B fluid. For

269 PS110, L has been estimated at 15.

270 For a multimode model, the extra stress may be expressed as a sum of contributions

271 from each mode. For the generalized multimode problem with N modes, each mode

272 (i) with partial viscosity (η_i) and relaxation time (λ_i), and the extra-stress tensor of the

273 FENE-CR expresses:

274
$$\underline{\underline{\boldsymbol{\sigma}}} = \sum_{i=1}^{N} g_i f_i(R_i)(\mathbf{A}_i - \mathbf{I}), \tag{8}$$

275 where $f_i(R_i) = 1/\left(1 - R_i/L_i^2\right)$ with $R_i = \mathrm{Tr}\left(\mathbf{A}_i\right)$. For simplicity, it is assumed that the

276 extensibility $L_i = L$ is constant, but other approaches may be used [Lielens et al.

277 (1998)]. The dimensionless evolution equation for the ith mode is

278
$$\frac{d\mathbf{A}_i}{dt} = -\frac{f_i(R_i)}{\mathrm{De}_i}(\mathbf{A}_i - \mathbf{I}), \tag{9}$$

279 Where $\overset{\nabla}{\mathbf{A}}_i = \frac{d\mathbf{A}_i}{dt} - \nabla\mathbf{v}^T_{\ i}\cdot\mathbf{A}_i - \mathbf{A}_i\cdot\nabla\mathbf{v}_i$ is the Oldroyd upper-convected time derivative of

280 A_i, and De_i is the Deborah number for the ith mode defined as follow

281
$$\mathrm{De}_i = \lambda_i / \tau \tag{11}$$

282 g_i and λ_i are the modulii and relaxation times described by the multimode

283 optimization see sub-section (2d) and where τ is the characteristic inertio-capillary

284 time scale of the system defined by $\tau = \sqrt{\rho R_0^3 / \gamma}$.

285 Scaling was performed using the piston radius R_0 as a length scale, and a

286 characteristic speed U as a velocity scale , where U is the average piston speed in the

287 2D case, and $U=R_0/\tau$ in the 1D case. The time was scaled by R_0/U and τ, in the 2D

288 and 1D cases respectively; whereas pressures and stresses were scaled by ρU^2. The

289 scalings yielded the dimensionless governing equations:

290
$$\frac{d\mathbf{v}}{dt} + (\mathrm{v}.\nabla)\mathbf{v} = -\nabla p + \frac{1}{\mathrm{Re}}\left(\nabla^2\mathbf{v} - \sum_{i=1}^{N} c_i \overset{\nabla}{\nabla A_i}\right) + \frac{1}{\mathrm{Fr}^2}\mathbf{z}, \qquad \nabla\cdot\mathbf{v} = 0, \tag{10}$$

291 where t, $\mathbf{v}$, and p are now the dimensionless time, velocity, and pressure

292 respectively. For each viscoelastic mode an additional parameter $c_i = g_i\lambda_i/\eta_s$ has been

293 introduced: it may be interpreted as a measure of the concentration (volume fraction)

294 of dumbbell molecules corresponding to the ith mode. With the particular scalings

295 used here, the flow is characterized by the dimensionless groups Re We, and Fr,

296 which are respectively the Reynolds, Weber, and Froude numbers

297
$$\mathrm{Re} = \frac{\rho U R_0}{\eta_s}, \quad \mathrm{We} = \frac{\rho U^2 R_0}{\gamma}, \quad \mathrm{Fr} = \left(\frac{U^2}{g R_0}\right)^{1/2}, \tag{13}$$

14

298   in addition to the Deborah number De_i for each mode, defined earlier. The Reynolds

299   number represents the competition between inertia and viscosity, the Weber number

300   the competition between the inertia and the surface tension while the Froude number

301   represents the competition between inertia and gravity effects.

302   Another important dimensionless number is that of Ohnesorge, $Oh = \eta_s / \sqrt{\rho \gamma R_0}$. With

303   the scalings used here, the Ohnesorge number can be expressed in terms of the Weber

304   and Reynolds numbers: $Oh = \sqrt{We} / Re$. Alternative choices of scaling may result in

305   other different dimensionless groupings [Eggers and Villermaux, (2008)] as for

306   example, the Capillary number (ratio between viscous forces and surface tension) and

307   the Bond number (ratio between gravitational forces and surface tension). The Bond

308   number and the Capillary number have been estimated at ~0.11 and between 0.04 and

309   0.28 respectively indicating that surface tension is the dominating force and the

310   gravitational effects negligible. An extensive discussion of dimensionless number of

311   the problem can be found in [McKinley, 2005b].

312   **3d. Computational methods**

313   **1D simulation**

314   The previous equations (4), (5), (6) can be further simplified to retrieve the lubrication

315   equation. The 1D simulation method follows the same approach than in the recently

316   presented published work by Tembely et al. (2012) namely considering the radial

317   expansions and taking the lower order results in r lead to the nonlinear one-

318   dimensional equations describing the filament dynamics [Eggers and Dupont (1994);

319   Shi et al. (1994)]. The result is a system of equations for the local radius h(z, t) of the

320   fluid neck, and the average velocity v(z, t) in the axial direction:

321 $$\partial_t h + v h' + v' \frac{h}{2} = 0 \tag{14}$$

322 where prime $(')$ denotes the derivative with respect to z coordinates and

323 $$\partial_t v + v v' = -\kappa' + 3\tilde{v}_s \frac{(v'h^2)'}{h^2} + \frac{1}{h^2}\left[h^2(\sigma_{p,zz} - \sigma_{p,rr}) \right]' \tag{15}$$

324 For the multimode one-dimensional model in dimensionless form, the axial and radial

325 stress may be expressed as:

326 $$\sigma_{p,zz} = \sum_{i=1}^{N} g_i f(R_i) A_{zz,i} \tag{16}$$

327 $$\sigma_{p,rr} = \sum_{i=1}^{N} g_i f(R_i) A_{rr,i} \tag{17}$$

328 As previously, the full expression of the curvature given in equation (18) was used to

329 avoid instability in the solution and to provide the capability to represent a rounded

330 drop:

331 $$\kappa = \frac{1}{h(1+h'^2)^{1/2}} - \frac{h''}{(1+h'^2)^{3/2}} \tag{11}$$

332 To close the one-dimensional model, the following boundary conditions are imposed,

333 the no-slip conditions at the piston surfaces,

334 $$h(z = -L/2, t) = h(z = L/2, t) = R_0 \tag{12}$$

335 $$v(z = -L/2, t) = -V_p, \; v(z = L/2, t) = V_p \tag{13}$$

336 and a kinematic condition for the radius h(z,t) of the jet may be expressed as

$$337 \qquad \frac{dh}{dt} = \frac{\partial h}{\partial t} + v_z \frac{\partial h}{\partial z} = v_r(r = h, t) \qquad (14)$$

338   The governing equations in 1D simulation were solved with COMSOL,

339   (http://www.uk.comsol.com/) using the Arbitrary Lagrangian-Eulerian (ALE)

340   technique. The ALE technique is such that the computational mesh can move

341   arbitrarily to optimize the shape of the elements, whilst the mesh on the boundaries

342   follows the pistons motion. This ALE capacity implemented in the Comsol code

343   combined with the choice of very fine meshes enables to track the relevant physics as

344   shown in (Tembely et al. 2012). Due to the piston motion the computational domain

345   changes with time (see Fig. 3). With the ALE approach, the time derivative of any

346   quantity is defined as $\frac{d}{dt} = \frac{\partial}{\partial t} + (\vec{v} - \vec{v}_m).\nabla$

347

348   where $\vec{v}_m$ is the mesh velocity imposed by the piston velocity.

349   It is worth mentioning that the stress boundaries are ignored in the 1D approach due

350   to the weakly viscoelastic character of the samples and the initial filament aspect ratio

351   being close to 1 [Yao and McKinley, 1998]. The 2D axisymmetric approach includes

352   per se that effect.

353   Fig. 4 presents the evolution of the simulated mid-filament as a function of time for

354   1D and 2D simulation using different number of mesh elements. The 1D numerical

355   results with between 240 and 3840 mesh elements do not show any difference. The

356   results thus seem to be insensitive to mesh size as shown in the figure below. Similar

357   observation is made for the 2D simulation results regardless of the initial number of

358   mesh elements. The 2D simulation approach mesh is adaptive and evolves with time

359   throughout the simulation resulting a very large number of elements (see insert in Fig.

360   4.a).

362 **2D simulation**

363 An extended version of the split Lagrangian-Eulerian method of Harlen et al [Harlen

364 et al. (1995)] was used. The nature of the extension was twofold: in the problems for

365 which the method was originally developed there were no free surface boundaries,

366 and the inertial terms were neglected (Re = 0). The method has since been adapted

367 and extended to deal with inertial flows and has been used to model the breakup of

368 Newtonian and viscoelastic jets [Morrison and Harlen (2010); Castrejon-Pita et al.

369 (2011)].

370 The velocity and pressure fields are discretized over an irregular triangular mesh of

371 P_1--P1 Galerkin elements; each component of the conformation tensor **A** is assigned

372 a value for each element. An artificial stabilization was employed in order to prevent

373 spurious numerical pressure oscillations [Brezzi and Pitkaranta (1984)]. The value of

374 the stabilization parameter was optimized with respect to the spectral properties of the

375 discrete coefficient matrix [Wathen and Silvester (1993)]. A theta-scheme was used

376 for the discrete time-stepping, and the discrete governing equations were linearized

377 via Picard iteration. For each iteration, the linear system was solved numerically using

378 the minimal residual (MINRES) method [Paige and Saunders (1975)]. Adaptive time-

379 stepping was controlled by a CFL [Courant et al. (1928)] condition. The position of

380 each mesh node was updated after each time-step using the converged velocity

381 solution.

382 The numerical integration of the evolution equation for the conformation tensor was

383 conducted separately for each element between time-steps, by transforming to a co-

384 deforming frame with local coordinates in each triangle. In such a frame, the upper

385 convected derivative $\overset{\triangledown}{\mathbf{A}}$ becomes the ordinary time derivative dA/dt. Similarly the

386 Lagrangian derivative D**u**/Dt becomes d**u**/dt. The interfacial boundary condition is

387 handled similarly to the treatment by [Westborg and Hassager (1989)].

388 To maintain element shape quality throughout the simulations, local mesh

389 reconnections were made between time-steps in regions where significant element

390 distortion had occurred. The criteria for reconnection were based on the geometric

391 optimality of the Delaunay triangulation [Edelsbrunner (2000)]. The local mesh

392 resolution was also maintained by the addition of new nodes in depleted regions, and

393 the removal of nodes in congested regions.

394 In order to represent the capillary breakup of thin fluid filaments, the fluid domain

395 was subdivided artificially when the filament radius falls below a certain threshold.

396 This threshold has been taken as $< 0.5\%$ of the piston diameter to match the smallest

397 diameter that can be experimentally resolved (~6μm). Below this value, the filament

398 is not experimentally visible and is therefore considered broken. A more detailed

399 discussion of the capability of the simulations to capture pinch-off dynamics on a

400 finer scale is given in [Castrejon-Pita et al. (2011)].

401

402 **4. Results and discussion**

403 **4.a Experimental results**

404 Examples of the base experimental data are shown in Fig. 5 where photographs of

405 Trimaster experiments for different polymer loading are shown as a function of time.

406 The pure DEP solvent, shown as series 5a, indicates a filament stretch followed by

407 end pinching during relaxation to give a single central drop. The other extreme is

408 shown by series 5d for the 5% polymer loading, where stretching is followed by a

409 progressive filament thinning with a very much longer break up time. The whole time

410 evolution of the full profile along the thread is of general interest and importance;

411 however the detailed behaviour of the centre line diameter will be considered

412 beforehand.

413 **4.b Numerical results**

414 **Mid filament evolution**

415 The experimental time evolution of the mid-point of the filament is given in Fig. 6

416 and the figure displays the characteristic feature of an increased filament life time

417 with a progressive increase of polymer loading. It is this experimental mid filament

418 time evolution that has been used as the basis for comparison with the 1D and 2D

419 numerical simulations. Fig. 7 shows that both the 1D and 2D numerical simulations

420 are in close agreement with the base case Newtonian experimental results. Both the

421 decay profile and final 7.5 ms break point are accurately described by the simulations.

422 Figures 7 to 15 present the evolution of the mid-filament and not the minimum

423 filament or the breakup point which position might vary from one case to another.

424 The simulation breakup diameter has been set at $6\mu m$ but might occur at the top and

425 bottom of the filament, as experimentally observed in the case of DEP. In such case,

426 a droplet is formed in the middle of the filament explaining the large diameter

427 observed experimentally and in simulations at breakup time (Fig. 5 and 7).

428 Single mode simulations are shown in Fig. 8, 9 and 10 for 1, 2.5 and 5%

429 concentration solutions respectively. The simulations were carried out using the

430 FENE-CR constitutive equation with the extensibility parameter L = 30. The

431 extensibility value of L = 30 adopted in this paper has been found to provide a better

432 match with the experimental results than the theoretic value of 15. The possible

433 existence of higher molecular mass chains, albeit in small quantities, may justify this

20

choice. Moreover, for an indication of the choice of L, the comparative plot depicted in Fig 13.b of the squared extensibility L^2 and $R_i = \text{Tr}(\mathbf{A}_i)$, which represents the average length per mode i.e. of the polymer chain, shows that an extensibility value of around 30 is an appropriate choice. The 5th mode seems to capture the polymer global chain unravelling mechanism which takes place at larger length scales. On the other hand, the others modes (1, 2, 3) with negligible values of R_i involves local changes of the molecular conformation. It's worth noting as well that the R_i axial evolution confirms that higher stretching occurs in the middle of the filament.

The capillary thinning of viscoelastic fluid is controlled by the longest relaxation time with a mid-filament diameter decreasing in the form of D(t) ~ α.exp(-t/3λ) [Bazilevsky et al. (1990)). Fitting this exponential decay to the experimental data presented in Fig. 6 yields extensional relaxation times λ$_{ext}$ of 0.425ms, 1.19ms and 3.2ms for 1, 2.5 and 5wt% respectively. The extensional relaxation λ$_{ext}$ increased with polymer loading as expected. Whilst both the 1D and 2D simulations match the 1% solution data shown in Fig. 8, there is a progressive mismatch in both decay and pinch off with increasing concentration shown in Fig. 9 and 10. In particular the decay immediately after piston cessation is over predicted by both 1D and 2D simulations. Perhaps surprisingly, both the 1D and 2D simulations give a similar response. It was speculated that differences may appear between single mode and multimode models because of the existence of shorter and longer modes and of their interactions close to capillary pinch-off in the vicinity of both pistons [Matallah et al. (2007)].

In the 1D paper, (Tembely et al., JOR 2012) single mode modelling only was used; however both a short mode obtained from the PAV data and a long mode obtained from matching with experiment were used. In that paper it was shown that the

458   smallest relaxation time as input in a non-linear model was unable to correctly predict

459   filament thinning whilst the longest relaxation time gave reasonable filament thinning

460   results but a large discrepancy with the experimental G' and G" data. In this paper,

461   incorporation of multi modes has been carried out in order to fit with greater accuracy

462   the filament thinning experimental results whilst also capturing the PAV data too. We

463   have chosen 5 modes in order to have one mode per decade over the range of interest

464   covered experimentally. The exact choice of the number of modes is a matter of

465   details to be emphasized. Two would be too few and eight probably too many.

466   In this paper, our objective is to predict, using the same non-linear constitutive

467   equation as in the previous paper, the results for extension solely from experimental

468   data measured in the linear viscoelastic regime. For that purpose, the oscillatory linear

469   viscoelastic data was then fitted to a multimode model with five modes spaced by a

470   decade between modes and the fitted parameters are given in Table II. These

471   multimode parameters were then used in both the 1D and 2D simulations using the

472   multimode FENE-CR constitutive equation (eq. 9 and 10). The results are shown in

473   Fig. 11, 12 and 14 for the 1, 2.5 and 5% solutions respectively. The fit at all

474   concentrations is now greatly improved from the single mode simulations over the

475   whole decay and again there appears to be little difference between the 1D and 2D

476   simulations.

477   Using a multimode Maxwell model approach allows better accounting for the

478   transition between visco-capillary thinning and elasto-capillary thinning as shown by

479   the large reduction of the swelling at time between 7 and 10ms. This constituted the

480   main limitation of the single mode Maxwell approach as shown in the previous

481   section and recently reported results by some authors of this paper (Tembely et al.

482   (2012)). The results appear to show clearly that a multimode description of the fluid is

483 necessary and that, perhaps surprisingly, the 1D simulation appears to give a closer

484 match to the experimental results. It is also to be emphasized that the multimode

485 approach allows retrieving the results for non-linear elongation solely with the help of

486 the linear time spectrum and the use of a constitutive equation. It is worth mentioning

487 that mathematically the fitting of the time constant is correct but often leads to poor

488 results, since the relaxation spectrum time are no longer well distributed, and the

489 longest time spectrum may become small. The choice we made by imposing the

490 relaxation time is well accepted and adopted in the literature when dealing with

491 multimode formulation of constitutive equations (see Bird et al…).

492 The sensitivity of the filament thinning and breakup to constitutive equation and non

493 linear parameters is shown in Fig. 14 and 15. In Fig. 14 it can be seen that using the

494 1D simulation, there is little difference between the multimode FENE-CR and

495 Oldroyd model predictions. Any differences that may appear were essentially masked

496 by the use of multi modes. Simulation using the theoretically predicted value for the

497 limiting extensibility L of PS110 (L = 15), the "best fit" obtained (L = 30) and a

498 significantly larger value, here L = 100, have been chosen to investigate the effect L

499 of the FENE-CR model. Fig. 14 shows that L does effect the simulation slightly in

500 the transition zone for the short time modes and particularly in the final stages of

501 decay with a pinch off time that decreases with decreasing limiting extensibility

502 parameter L.

503 **Transient profiles**

504 Figure 16 and 17 present the1D and 2D multi modes FENE-CR and Oldroyd-B full

505 simulated transient profiles for the case of 5wt% PS110 diluted in DEP. A generally

506 good match between simulations is observed with differences only appearing towards

23

507   the end of the filament thinning mechanism, ie, near to break up. Figure 16 shows

508   that the 1D simulation predicts a final thread like decay, whereas the 2D simulation

509   still has a pinch off component. The multi mode Oldroyd-B simulations shown in

510   Figure 17 also show a similar trend, with the 1D having a more thread like final

511   decay. Despite the improvement provided by the use of multi modes approach instead

512   of the single mode approach, these results clearly highlight the need for investigating

513   other constitutive equations for the modelling of fast stretching and filament thinning

514   of low viscoelastic fluids.

515   Detailed full profile comparison between experimental transient profiles of PS110 at

516   5wt% in DEP with FENE-CR multi modes 1D and 2D simulation transient profiles is

517   presented in Fig. 18. Both simulation approaches provide a good match with the

518   experimental profiles for the overall mechanism with again the main discrepancies

519   appearing at the late stage of the filament thinning mechanism. Close examination of

520   the experimental and simulated profiles show that the fluid regions attached to the top

521   and bottom pistons are smaller experimentally than for both simulations. This results

522   in a larger length of the thinning filament in the experimental case and may explain

523   the differences observed between 1D and 2D simulations. The filament aspect ratio is

524   usually defined by the variation between initial and final position of the piston but it

525   can be seen here that despite using similar piston motions for the simulations and the

526   experiments, differences in the filament length arise. Such filament length variations

527   are expected to significantly affect the filament break up profile especially in the case

528   of low viscosity low viscoelastic fluids. The investigation of the full velocity field, in

529   terms of simulation and using Particle Image Velocimetry (PIV) experiments, within

530   both the filament and the piston region would help the understanding of the

531   differences observed in the filament shape especially toward the break up time.

532

Weissenberg number W_i and apparent extensional viscosity $\eta_{e,app}$

534 Figure 19 presents the evolution of the Weissenberg number W_i as a function of the

535 filament thinning Hencky strain ε in the case of multi mode FENE-CR simulations.

536 Weissenberg number and filament thinning Hencky strain may be defined as follows:

537
$$W_i = \lambda_{ext} \, \dot{\varepsilon} \tag{22}$$

538
$$\varepsilon = 2 \ln \left(\frac{D_0}{D(t)} \right) \tag{23}$$

539
$$\dot{\varepsilon} = - \frac{2}{D(t)} \frac{dD(t)}{dt} \tag{24}$$

540 The simulated data of the mid filament evolution have been used to estimate the

541 longest extensional relaxation time and value of 2.98ms and 5.1ms were obtained for

542 the 1D approach and the 2D simulation respectively, in the case of PS110 at 5wt% in

543 DEP.

544 In the case of the multimode FENE-CR approach, the 1D simulation approach

545 predicts reasonably well the overall mechanism with; in particular the double curved

546 behaviour experimentally observed in the transition between visco-capillary and

547 elasto-capillary regimes ($W_i = 0.5$) whereas the 2D approach provides a good match

548 on the long time scale but does not capture the double curvature. The behaviour at

549 high Hencky strain is correctly represented for both types of simulations.

550 The use of the multimode approach does significantly improve the match with

551 experimental data in comparison to that of the single mode and, even if all the

552 subtleties of the complex filament thinning mechanism seem not to be fully

553 represented, it provides good agreement with experimental data. The description of a

554   Weissenberg number, when using a multimode approach, has difficulties in relation to

555   a suitable choice of relaxation time used in the definition of the Weissenberg number.

556   It is also very sensitive to noise (simulation or experimental) due to the fact that it is

557   based on the derivative of the mid filament evolution.

558   Finally, Fig. 20 presents the transient apparent extensional viscosity $\eta_{e,app}$, with

559   $\eta_{e,app} = -\sigma \frac{dt}{dD_{mid}(t)}$, as a function of Hencky strain for multimode FENE-CR. The

560   comparison is particularly good in view of the approximations which have been made

561   for the calculation of the phenomenological Maxwell times. Notably, the complex

562   behaviour of the extensional viscosity is qualitatively correctly predicted at

563   intermediate times by both the 1D and 2D simulations with the prediction of the

564   sudden increase in η_{ext} after the pistons have stopped. Close attention shows that the

565   1D simulation approach produces a surprisingly good agreement with experimental

566   results, while the 2D simulation approach fails to represent the long term extensional

567   viscosity behaviour.

568   The relative better accuracy of the 1-D model may be due to the combined effect of

569   the ALE technique, for free surface tracking, together with the expression of the full

570   curvature providing means for representing a fully rounded drop. These features

571   together with the low stretching speed, used in this work, enables the 1D model to

572   exhibit quite good results compared to the 2D as previously pointed out by [Yildirim

573   and Basaran, 2001]. Indeed, finding stable discretisation schemes for 2D models

574   prove to be most challenging for free surface problems and are computationally more

575   intensive, (almost 2 to 3 orders of magnitude compared to 1D models). Finally the

576   treatment of the tri-junction line (contact between solid/liquid/air) which plays a non-

577   negligible role in the vicinity of pistons is not well-resolved, and this may have a

578 larger effect for the 2D model compared to the 1D model therefore affecting its

579 overall performance.

580

581 **5. Conclusions**

582 Results described in this paper have shown that a multimode constitutive equation

583 approach greatly improves the detailed prediction of viscoelastic extensional flow

584 behaviour of dilute or semi dilute polymer solutions. The result is consistent with the

585 findings of Entov and Hinch (1997) who also found it necessary to resort to a

586 multimode mode approach for higher viscosity viscoelastic polymer solutions.

587 However, simulations for different polymer concentrations indicate that the

588 improvement due to the use of multimodes instead of single mode is reduced with the

589 increase of the solution concentration.

590 The FENE-CR constitutive equation appears to be an effective suitable constitutive

591 equation to use for the fluids examined in this paper, although the Oldroyd model was

592 found to give an equivalent response when used with multimodes. It appears that

593 multimode modelling can disguise certain limiting features of different constitutive

594 models, but however remains necessary even for the monodisperse polymer systems

595 which have been tested. The fitting of numerical simulation to the experimental

596 results was not perfect and this can be attributed to both experimental factors and also

597 weaknesses in the choice of constitutive equations used. This highlight that more

598 physics, or a new set of constitutive equations, needs to be incorporated in the

599 simulations for them to quantitatively match the experimental data.

600 To be specific on this aspect, more sophisticated models such as the one with

601 elaborate closure relationships for FENE models (Lielens et al. 1998) or the multi-

602 mode Pom Pom model taking into account molecular topology (McLeish & Larson,

603 1998) need to be tested. Additional experiments are also needed in order not to have

604 too many adjustable parameters.

605 An initially surprising result of the paper is the fact that the 1D modelling gives better

606 results than 2D modelling in some limited cases described above. This indicates that

607 the 1D approximation is valid enough for the initial and boundary conditions used and

608 in particular for the mid filament diameter evolution. It is possible (probable?) that

609 when details of highly non-linear behaviour, i.e. pinch off position, number of beads,

610 etc. are considered differences may emerge from the two techniques. The pinch off

611 position and the number of small drops is an essential parameter in ink-jet printing

612 since the satellite drops may merge or not following the type of detachment.

613

614 Further comparison would be to follow the filament transients following breakup.

615 Such a work has been done for Newtonian liquid (Castrejon Pita et al. 2012) but this

616 work does not include non-Newtonian fluids. The non-linear evolution of main drop

617 and satellites do influence printability criterion taking into account the Ohnesorge and

618 the Deborah numbers as described in preliminary work by Tembely et al. 2011.

619

620

629

630

632 **References**

633 Anna, S. L., and G. H. McKinley, "Elasto-capillary thinning and breakup of model

634 elastic liquids," J. Rheol.45, 115–138 (2001).

635 Bach, A., H. K. Rasmussen, P-Y. Longin, and O. Hassager, "Growth of non-

636 axisymmetric disturbances of the free surface in the filament stretching rheometer:

637 Experiments and simulation," J. Non-Newtonian Fluid Mech. 180, 163–186 (2002).

638 Bazilevsky A. V., V. M. Entov and A.N. Rozhkov, "Liquid filament microrheometer

639 and some of its applications", Third European Rheol. Conf., (Ed. D.R. Oliver)

640 Elsevier Applied Science, 41-43 (1990)

641 Bazilevsky A.V., V.M. Entov and A.N. Rozhkov, "Failure of polymer solutions

642 filaments", Pol. Sc. Series B, **39**, 316-324 (1997)

643 Bhat, P. P., S. Appathurai, M. T. Harris, M. Pasquali, G. H. McKinley, and O. A.

644 Basaran, "Formation of beads- on-a-string structures during break-up of viscoelastic

645 filaments," Nat. Phys. 6, 625–631 (2010).

646 Castrejon-Pita, J. R., N. F. Morrison, O. G. Harlen, G. D. Martin, and I. M.

647 Hutchings, "Experiments and Lagrangian simulations on the formation of droplets in

648 continuous mode," Phys. Rev. E 83, 016301 (2011).

649 Castrejon-Pita, A. A., J.R.Castrejon-Pita and I.M. Hutchings, "Breakup of liquid

650 filaments", Physic Review Letter, 108, 074506 (2012)

651 Chilcott, M. D., and J. M. Rallison, "Creeping flow of dilute polymer solutions past

652 cylinders and spheres," J. Non-Newtonian Fluid Mech. 29, 381–432 (1988).

Clasen C., J.P. Plog, W.-M Kulicke, M. Owens, C. Macosko, L.E. Scriven, M. Verani and G.H. Mckinley, "How dilute are dilute solutions in extensional flows?", J. Rheol., **50(6)**, 849-881 (2006a)

Clasen, C., J. P. Plog, W.-M.Kulicke, M. Owens, C. Macosko, L. E. Scriven, M. Verani, and G. H. Mckinley, "How dilute are dilute solutions in extensional flows?," J. Rheol. 50(6), 849–881 (2006b).

Courant R., K. Friedrichs and H. Lewy, "Über die partiellenDifferenzengleichungen der mathematischenPhysik", Math. Ann. 100 32-74 (1928)

Crassous, J., R. Re´gisser, M. Ballauff, and N. Willenbacher, "Characterisation of the viscoelastic behaviour of complex fluids using the piezoelastic axial vibrator," J. Rheol.49, 851–863 (2005).

Dong H., W.W. Carr and J.F. Morris, "An experimental study of drop-on-demand drop formation", Phys. Fluids, **18**, 072102-1/072102-16 (2006)

Eggers J., "Nonlinear dynamics and breakup of free-surface flows", Rev. Mod. Phys., **69**, 865-929 (1997)

Eggers, J., and T. F. Dupont, "Drop formation in a one-dimensional approximation of the Navier-Stokes equation," J. Fluid Mech. 262, 205 (1994).

Entov V.M. and E.J. Hinch, "Effect of a spectrum relaxation times on the capillary thinning of a filament elastic liquids", J. Non-Newtonian Fluid Mech., **72**, 31-53 (1997)

Ferry, J. D., Viscoelastic Properties of Polymers (John Wiley & Sons Inc., 1980).

674 Fontelos, M. A., and J. Li, "On the evolution and rupture of filaments in Giesekus and
675 FENE models", J. Non- Newtonian Fluid Mech. 118, 1–16 (2004).

676 Furlani E.P. and M. S. Hanchak, "Nonlinear analysis of the deformation and breakup
677 of viscous microjets using the method of lines", E. P. Furlani & M. S. Hanchak, Int. J.
678 Numerical Methods in Fluids 65(5), 563-577 (2011)

679 Furlani E.P., "Temporal instability of viscous liquid microjets with spatially varying
680 surface tension", J. Phys. A: Math. Gen., **38**, 263 (2005)

681 Graessley, W. W., "Polymer chain dimensions and the dependence of viscoelastic
682 properties on the concentration, molecular weight and solvent power," Polymer **21**,
683 258–262 (1980)

684 Groß, T., L. Kirschenmann, and W. Pechhold, "Piezo axial vibrator (PAV)—A new
685 oscillating squeeze flow rheometer," in Proceedings Eurheo edited by H. Munsted, J.
686 Kaschta, and A. Merten (Erlangen, 2002).

687 Hoath S.D., G.D. Martin, T.R. Tuladhar, M.R. Mackley, I. Hutching and D. Vadillo,
688 "Link between ink rheology, drop-on-demand jet formation and printability", J.
689 Imaging Sci. Tech. (in press), **53**, **4**, 041208–041208-8 (2009).

690 Jang D., D. Kim and J. Moon, "Influence of fluid physical properties on ink-jet
691 printability", Langmuir, **25**, 2629-2635 (2009)

692 Kamath V. and M.R. Mackley.,"The rheometric characterization of flexible chain and
693 liquid crystal polymers",3rd European Rheology Conf., British Society of Rheology,
694 Ed. D.R. Oliver, 261-264, (1990).

695 Kirschenmann, L., Ph.D. thesis, Institut fur dynamischematerialprunfung (IdM),
696 University of Ulm, (2003).

G. Lielens, P. Halin, I. Jaumain, R. Keunings, and V. Legat. New closure approximations for the kinetic theory of finitely extensible dumbbells. J. Non-Newtonian Fluid Mech., 76:249–279, 1998.

Matallah, H., K. S. Sujatha, M. J. Banaai, and M. F. Webster, "Single and multi-mode modelling for filament stretching flows," J. Non-Newtonian Fluid Mech. 146, 92–113 (2007).

McKinley G.H and G.H. and Sridhar T., "Filament Stretching Rheometry of Complex Fluids", Annual Rev. Fluids Mech., **34**, 375-415 (2002)

McKinley G.H., "Visco-Elastic-Capillary thinning and break-up of complex fluid", Rheology Reviews 2005, The British Soc. Rheol., 1-49 (2005a)

McKinley G.H, "Dimensionless groups for understanding free surface flows of complex fluids", Soc. Of Rheo. Bulletin, (2005b).

McLeish, T.C.B. and R.G. Larson, 1998, "Molecular constitutive equations for a class of branched polymers: The pom-pom polymer, J. Rheol. **42**, 81-110.

Morrison, N. F. and O. G. Harlen, "Viscoelasticity in inkjet printing," Rheol. Acta, 49, 619–632 (2010).

Orr N.V., T. Sridhar, "Probing the dynamics of polymer solutions in extensional flow using step strain rate experiments", J. Non-Newtonian Fluid Mech., **82**, 203-232 (1996)

Rodd, L.E., T.P. Scott, J.J. Cooper-White and G.H. McKinley, "Capillary Breakup Rheometry of Low-Viscosity Elastic Fluids", Appl. Rheol., **15** (1), 12-27, (2005).

Tembely M., D.C. Vadillo, M.R. Mackley and A. Soucemarianadin, "The matching of a "one-dimensional" numerical simulation and experiment results for low viscosity

Newtonian and non-Newtonian fluids during fast filament stretching and subsequent break-up", J. Rheol. 56, 159-184 (2012)

Moussa Tembely1, Damien Vadillo2, Malcolm R. Mackley2 and Arthur Soucemarianadin1, "Towards an Optimization of DOD Printing of Complex Fluids, Non Impact Printing Conference, Salt Lake City, Utah (2011)

Vadillo, D. C., Mathues, W., Clasen, C., "Microsecond relaxation processes in shear and extensional flows of weakly elastic polymer solutions", Rheol. Acta **51** (2012).

Vadillo, D. C., T. R. Tuladhar, A. C. Mulji, S. Jung, S. D. Hoath, and M. R. Mackley, Evaluation of the inkjet fluid's performance using the 'Cambridge Trimaster' filament stretch and break-up device," J. Rheol. 54(2), 261–282 (2010a).

Vadillo, D. C., T. R. Tuladhar, A. Mulji, and M. R. Mackley, "The rheological characterisation of linear viscoe-elasticity for ink jet fluids using a piezo axial vibrator (PAV) and torsion resonator (TR) rheometers," J. Rheol. 54(4), 781–799 (2010b).

Yao M. and G.H. McKinley, "Numerical simulation of extensional deformations of viscoelastic liquid bridges in filament stretching devices", J. Non-Newtonian Fluid Mech., 74, 47-88 (1998).

Yildirim, O. E., and O. A. Basaran, "Deformation and breakup of stretching bridges of Newtonian and shear- thinning liquids: Comparison of one- and two-dimensional models," Chem. Eng. Sci. 56(1), 211–233 (2001).

Solvent	M_w (g/mol)	C (wt%)	η^* (mPa.s)
DEP	110000	0	10
DEP	110000	1	15.2
DEP	110000	2.5	31.5
DEP	110000	5	69

742   Table I: Zero shear rate complex viscosity of the different polymer solutions at 25°C

743

744

l_i(µs)	1%PS	2.5%PS	5%PS	10%PS
	g_i(Pa)	g_i(Pa)	g_i(Pa)	g_i(Pa)
1	7.789	83.8229	397.9015	1086.4419
10	428.76	1450.8952	4680.9517	9126.8723
100	1.6435	10.5177	93.1172	2012.6511
1000	0	0	0	16.4133
10000	0.0342	0.1855	0.4288	0.4291

745   Table II: Relaxation time and shear modulus obtained from Maxwell model fit of the

746   PAV data for the different samples

747
748

751
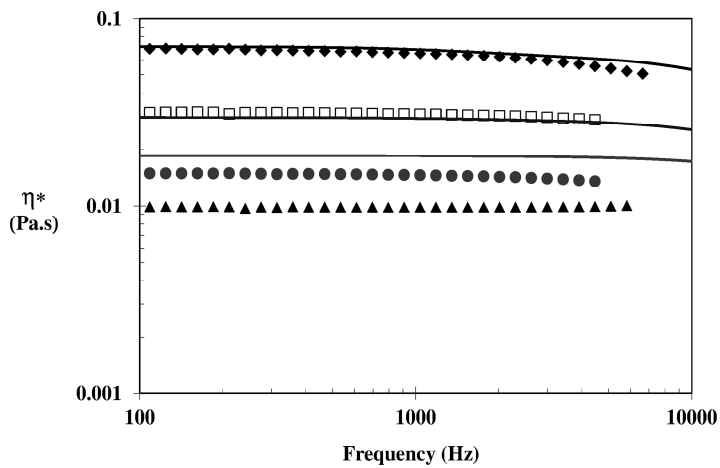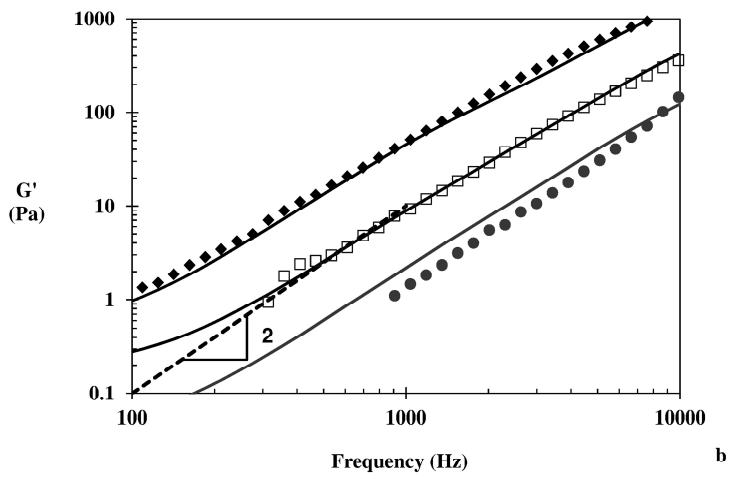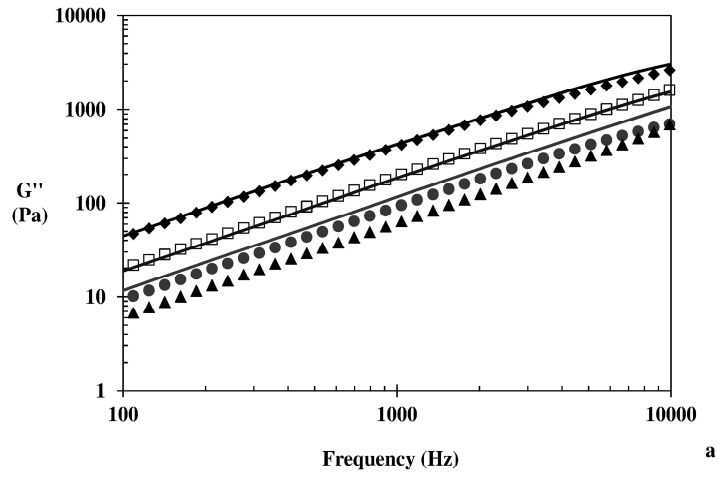
Figure 1: Evolution of (a) Loss modulus G'', (b) elastic modulus G' and (c) complex

viscosity h* as a function frequency for DEP-PS 110 000 solutions at different

concentrations. (▲) DEP, (●)DEP-1wt% PS110, (□) DEP-2.5wt% PS110, and (♦)

DEP-5wt% PS110. Solid line represents the multimode optimization results while the

dashed line on G' graph corresponds to a power law function of index 2.

757
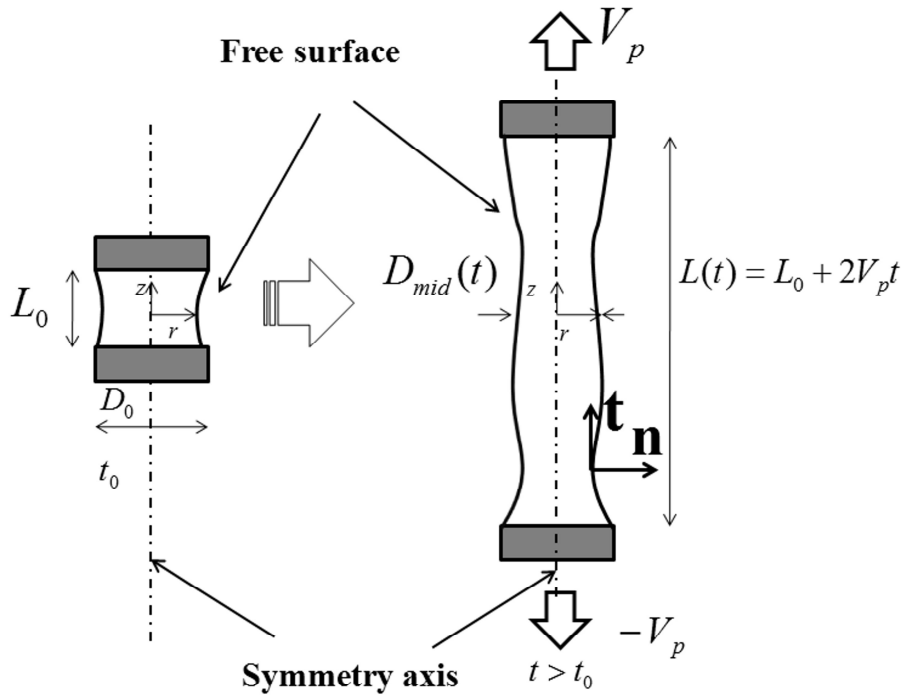
Figure 2: Diagram of filament stretch and thinning geometry and the computational domain, shown midway through the stretching phase as the pistons move outwards and the fluid column necks in the middle. Initially the fluid column is cylindrical. Extracted from [Tembely et al., 2012]

766

767
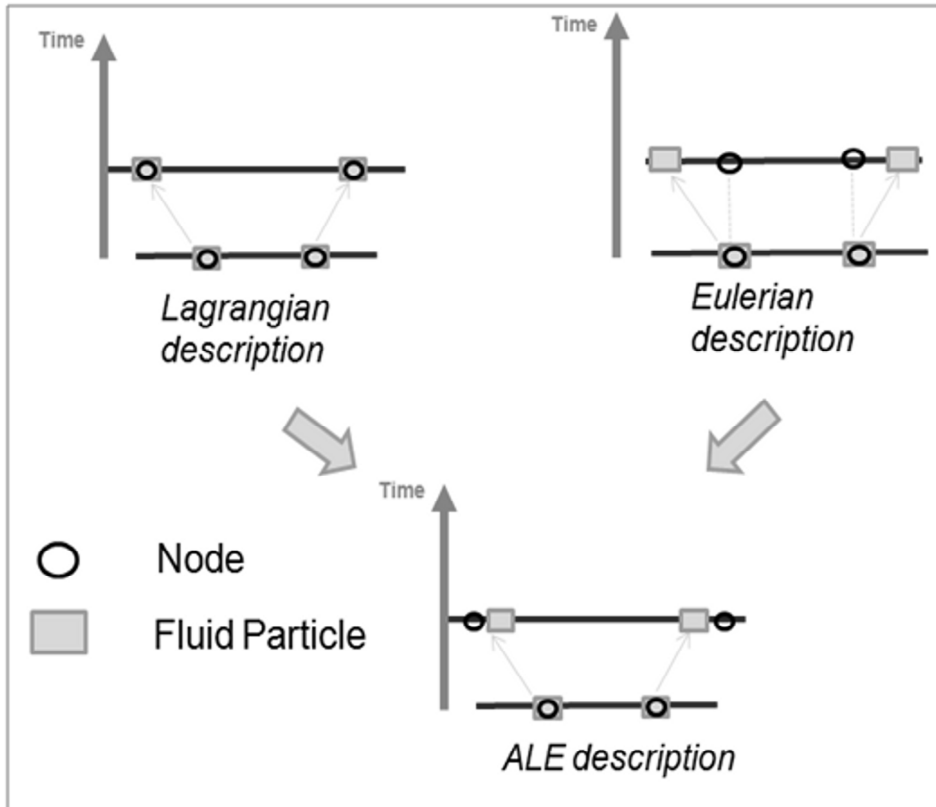
Figure 3: mesh evolution of the ALE method for the 1D simulation

769
770
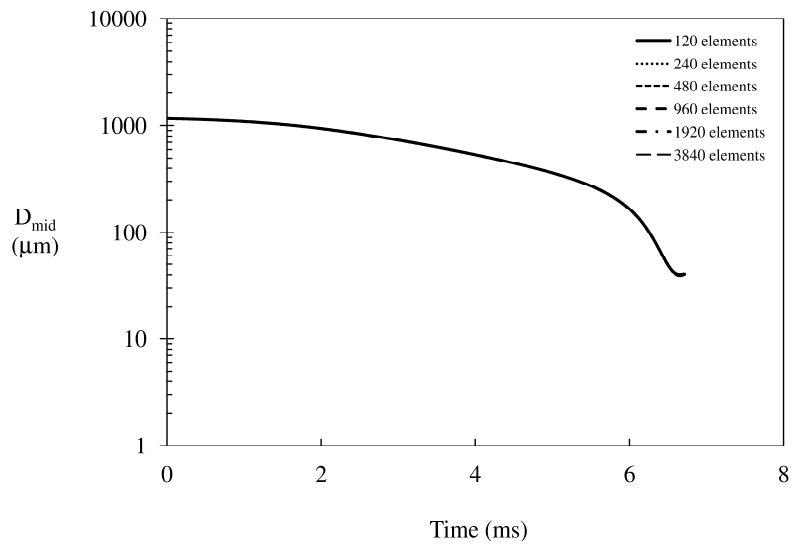
a
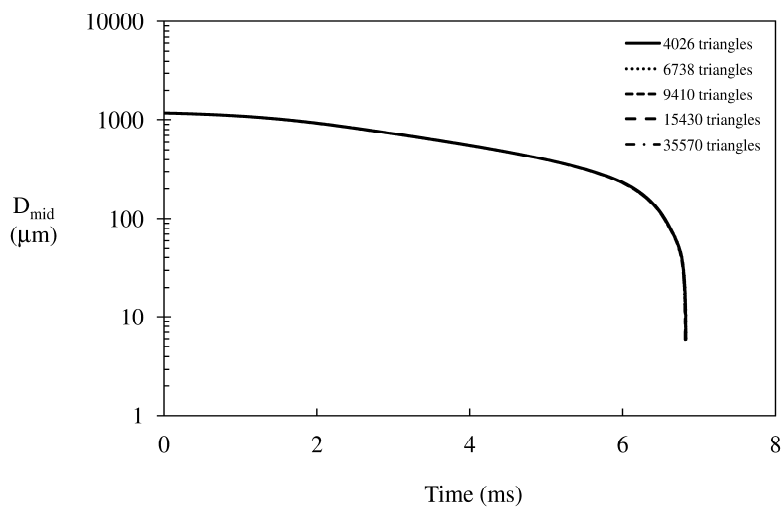
b

771
772
773 **Figure 4**: Evolution of the simulated mid-filament for different number of mesh

774 elements for (a) 1D simulation approach with the transient profile at t = ms in insert

775 and (b) 2D simulation approach with the mesh example in the 35570 triangles case in

776 insert. In the 2D simulation, the number of triangles is the one at t = 7.2ms.

777

778

779
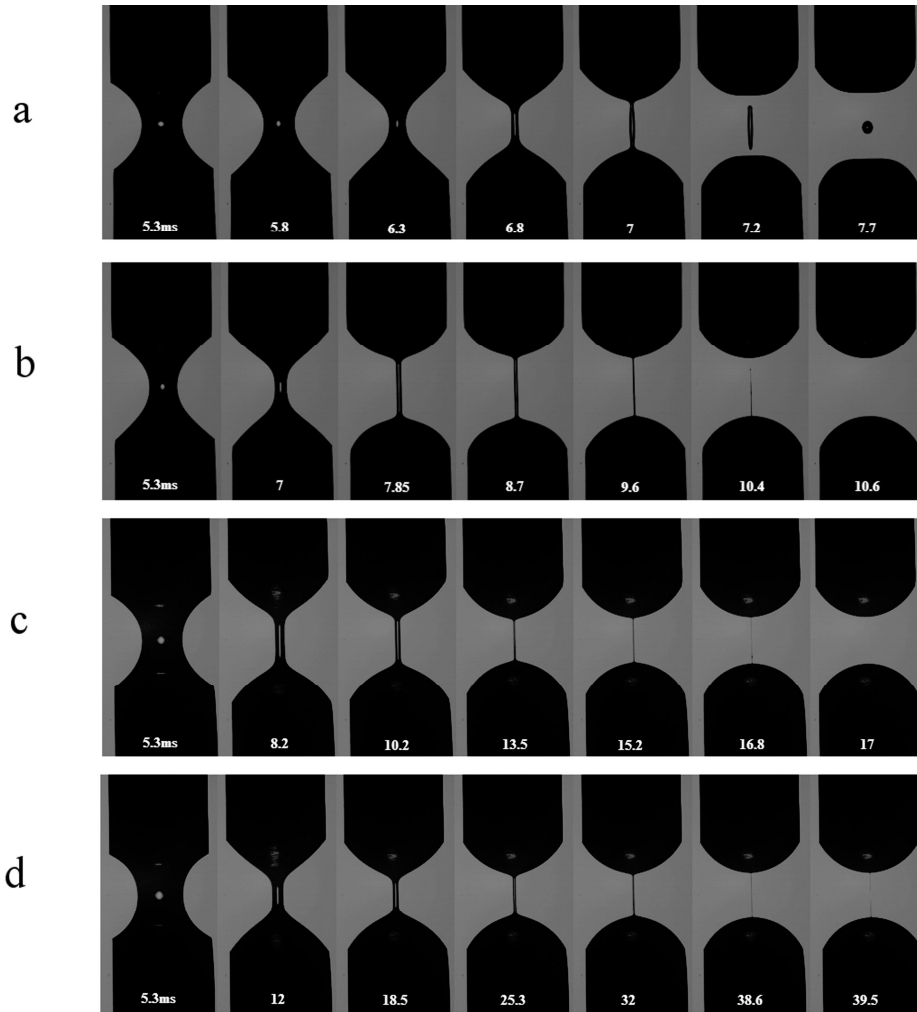
Figure 5: Photograph of the filament stretch, thinning and break up captured with the Trimaster for (a) DEP, (b) DEP + 1wt% PS110, (c) DEP + 2.5wt% PS110, (d) DEP + 5wt% PS110. The first picture of each series (t = 5.3ms) corresponds to the piston cessation of motion

784
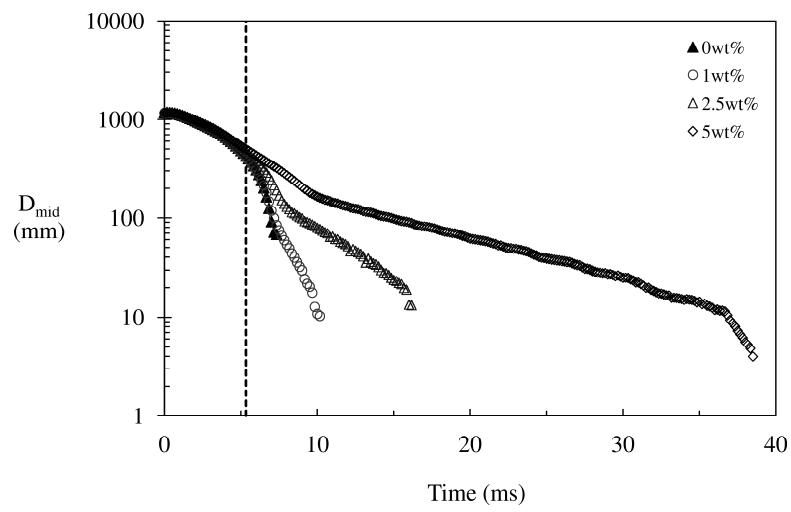
Figure 6: Time evolution of mid-filament taken from photographs of figure 2. (▲) DEP, (○) DEP-1wt% PS110, (Δ) DEP-2.5wt% PS110, and (♦) DEP-5wt% PS110, (---) piston cessation of motion.

791
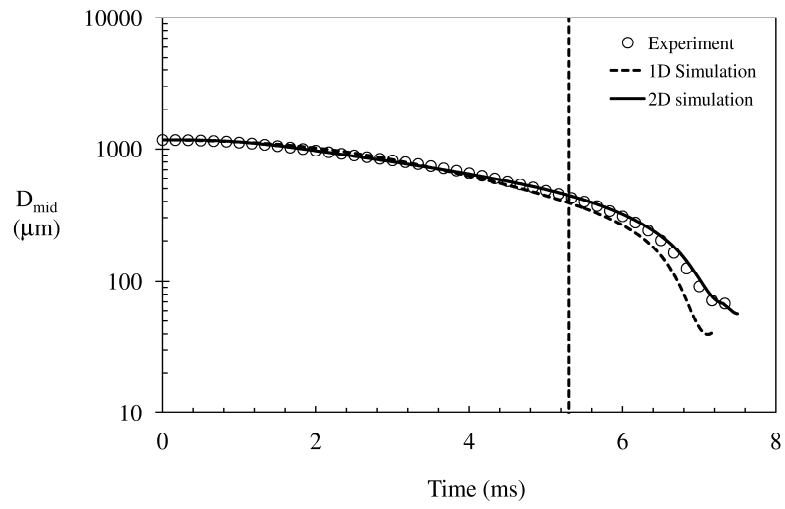
Figure 7: Newtonian base case. Plot of the mid filament diameter evolution as a

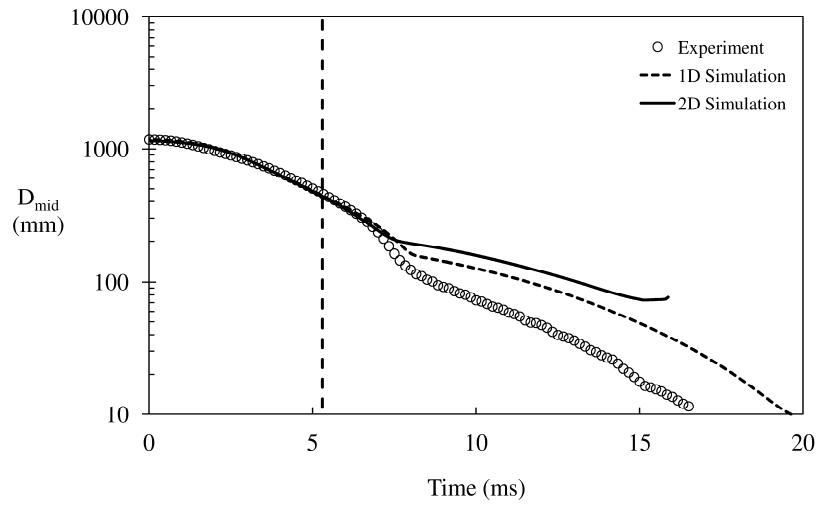function of time. Vertical line (---) corresponds to piston cessation of motion.

794
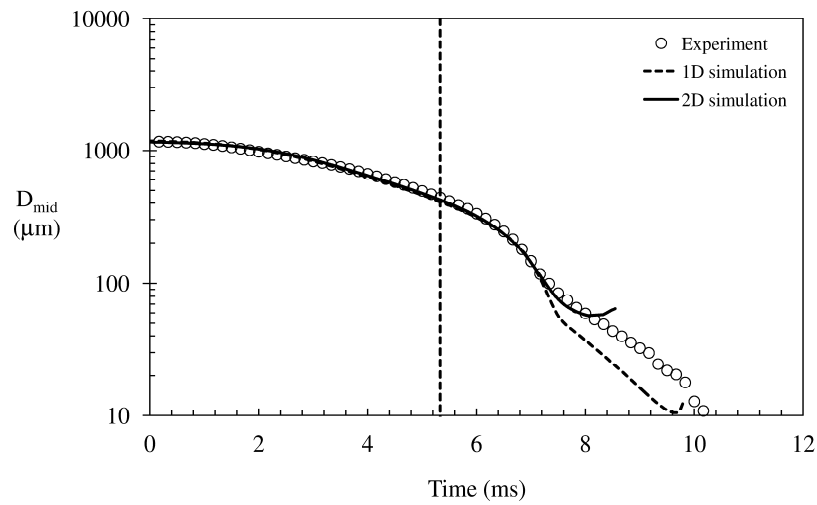
797 **Figure 8:** Single mode, 1wt% PS110 in DEP solution. Plot of the mid filament

798 diameter evolution as a function of time. Constitutive equation: Fene-CR, relaxation

799 time λ = 0.425ms, shear modulus g = 11.25Pa and polymer extensibility L = 30.

800 Initial gap size: 0.6mm, final gap size: 1.4mm, pistons relative velocity: 150mm/s.

801 Vertical line (---) corresponds to piston cessation of motion (aspect ratio 2.3).
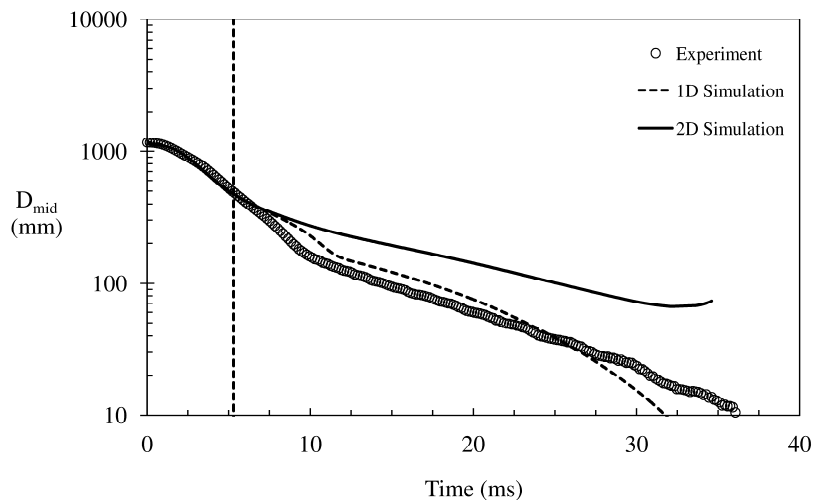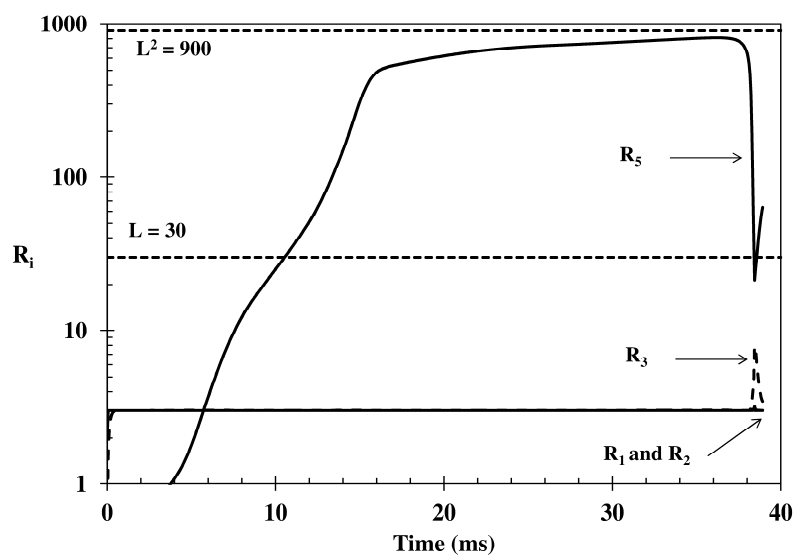
802

803
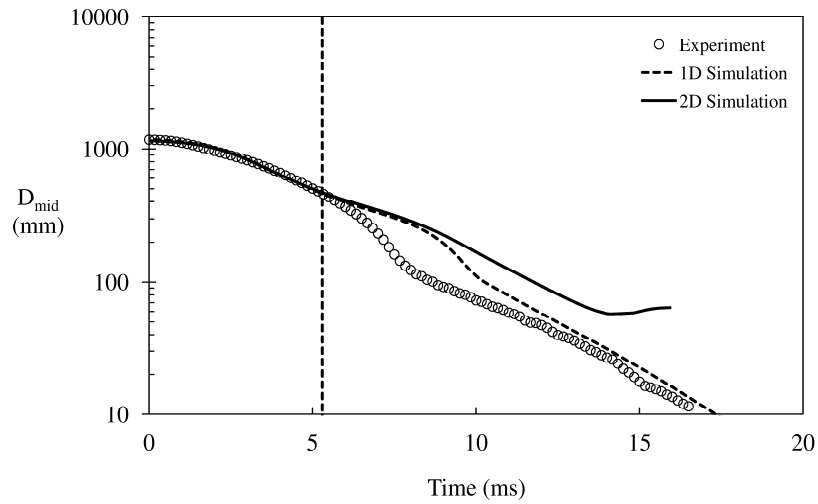
804

805 **Figure 9:** Single mode, 2.5wt% PS110 in DEP solution. Plot of the mid filament

806 diameter evolution as a function of time. Constitutive equation: Fene-CR, relaxation

807 time λ = 1.19ms, shear modulus g = 15Pa and polymer extensibility L = 30. time (---)

808 corresponds to piston cessation of motion.

809
810

811
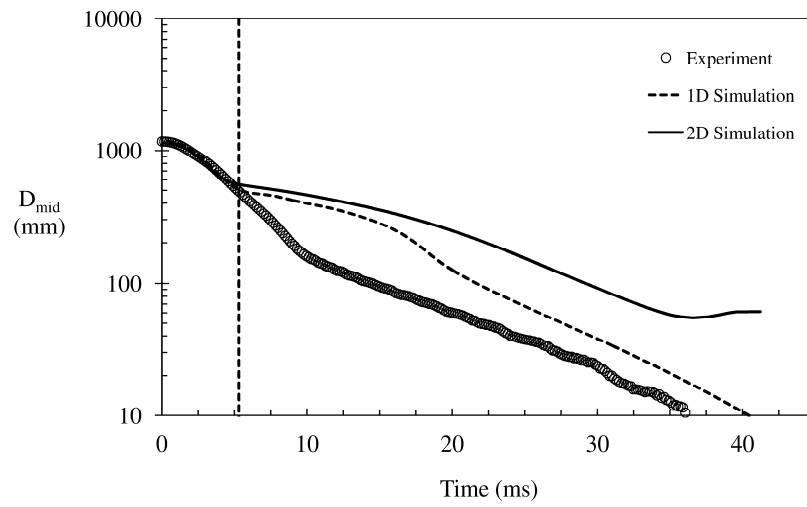
Figure 10: Single mode, 5wt% PS110 in DEP solution. Plot of the mid filament

diameter evolution as a function of time. Constitutive equation: Fene-CR, relaxation

time λ = 3.2 ms, shear modulus g = 17Pa and polymer extensibility L = 30.   Vertical

Line (---) corresponds to piston cessation of motion.

816

817
818
819
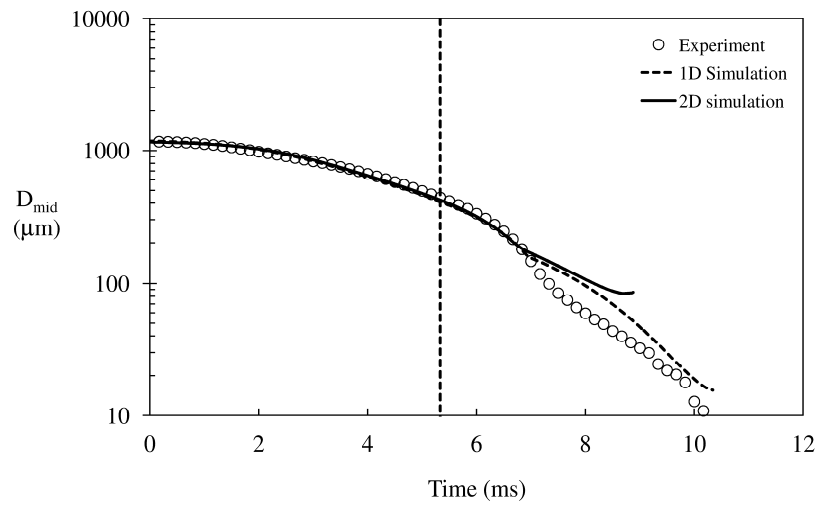
Figure 11: Multi mode, 1wt% PS110 in DEP solution. Plot of the mid filament

diameter evolution as a function of time. Constitutive equation: Fene-CR, relaxation

times λ_i and shear modulus g_i for the different modes i are given in Table II and

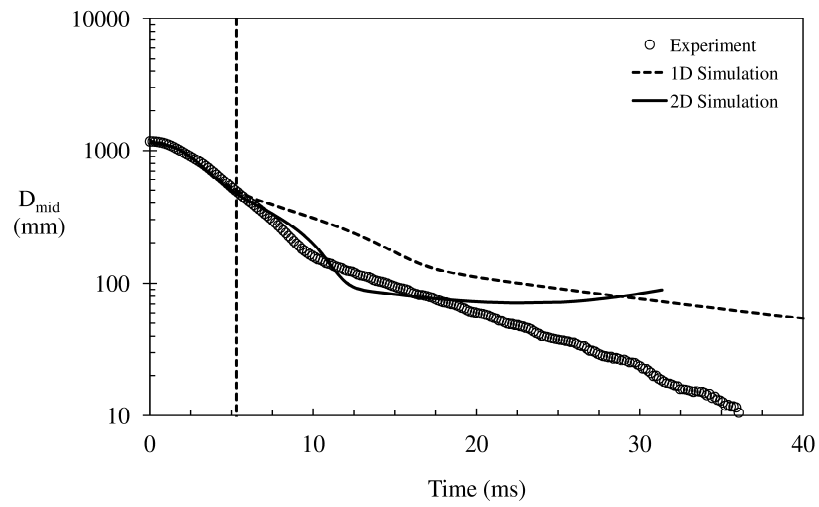polymer extensibility L = 30. Vertical line (---) corresponds to piston cessation of

motion.

825

Figure 12: Multi mode, 2.5wt% PS110 in DEP solution. Plot of the mid filament

diameter evolution as a function of time. Constitutive equation: Fene-CR, relaxation

times λ_i and shear modulus g_i for the different modes i are given in Table II and

polymer extensibility L = 30. Vertical line (---) corresponds to piston cessation of

motion.

835

a

b

836

Figure 13: (a) Multi mode, 5% solution. Plot of the mid filament diameter evolution

as a function of time. Constitutive equation: Fene-CR, relaxation times λ_i and shear

modulus g_i for the different modes i are given in Table II and polymer extensibility L

840   = 30. Vertical line (---) corresponds to piston cessation of motion. (b) Evolution of

841   the R_i as a function of time

842

843

844

Figure 14: Multi modes, 5wt% PS110 in DEP solution. Plot of the mid filament

diameter evolution as a function of time. Constitutive equation: Oldroyd-B, relaxation

times λ_i and shear modulus g_i for the different modes i are given in Table II. Vertical

line (---) corresponds to piston cessation of motion.

849
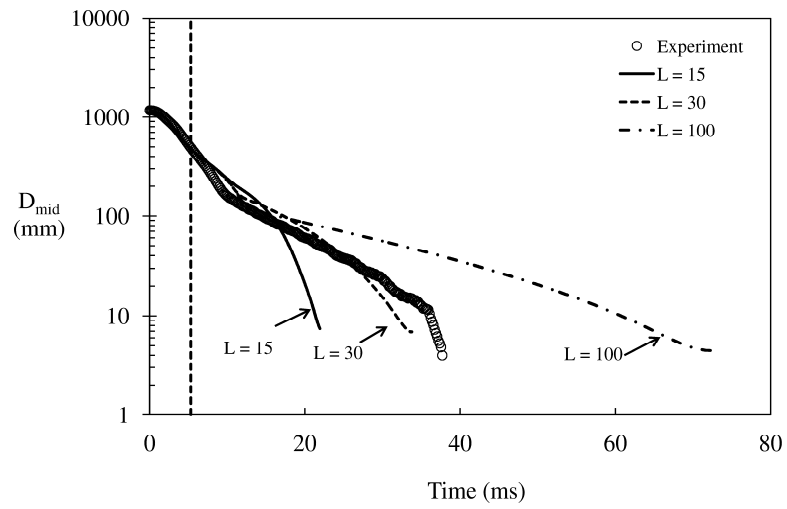
850

851

852   **Figure 15:** Effect of extensibility parameter L. Symbols represent the experimental

853   data of the evolution of the mid-filament as a function time and lines represent 1D

854   multi-mode numerical simulations for different polymer chain extensibilities L.

855   Constitutive equation: Fene-CR , relaxation times λ_i and shear mdulus g_i for the

856   different modes i are given in Table II..   Vertical line (---) corresponds to piston

857   cessation of motion.

858
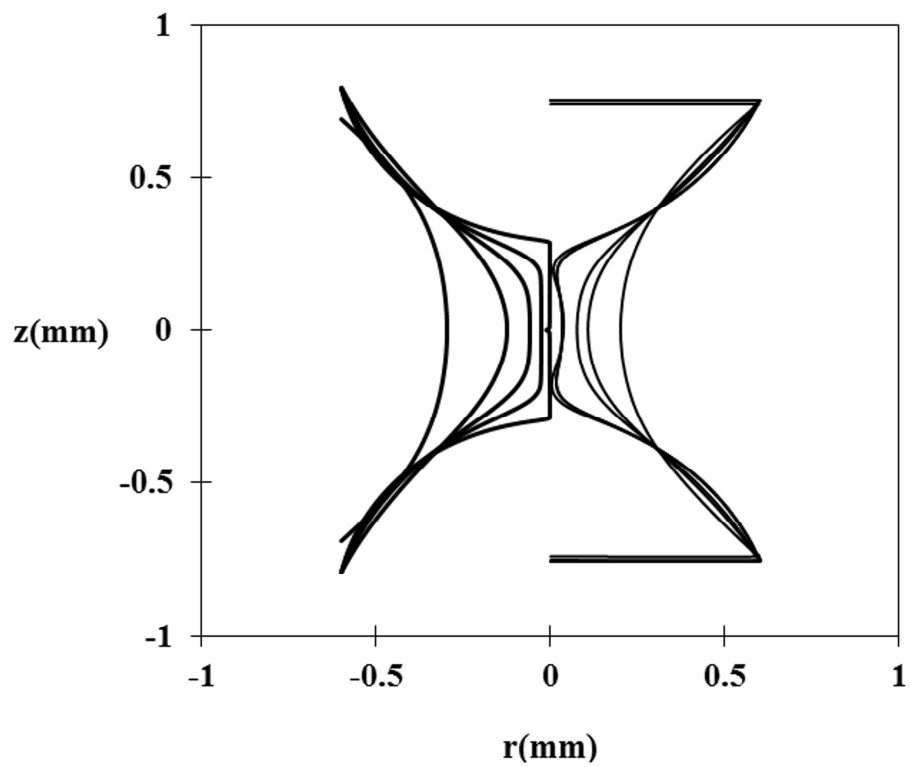
Figure 16: Comparison between the 1D numerical FENE-CR multimode transient
profiles (left), and the corresponding 2D simulations (right) for the DEP+5%PS. The
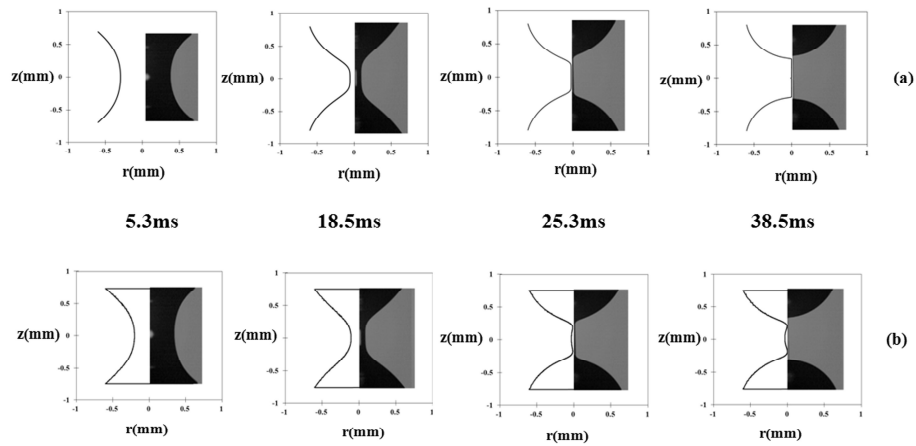prescribed times are 5.3ms, 12ms, 18.5ms, 25.5 ms, 38ms.

866
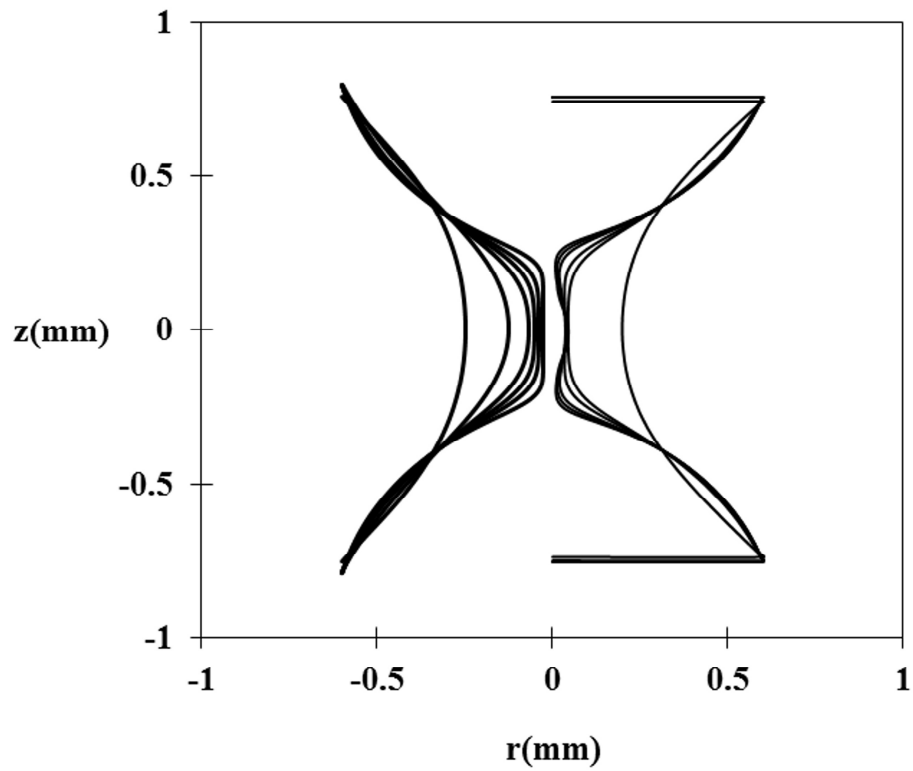
Figure 17: A comparison between the 1D numerical Oldroyd-B multimode transient

profiles (left), and the corresponding 2D simulations (right). The prescribed times are

5.3ms, 12ms, 18ms, 25ms, 32ms and 44ms for 1D simulation and 5.3ms, 12ms, 18ms,

25ms, 28ms, 32.5ms for 2D simulation

871
872

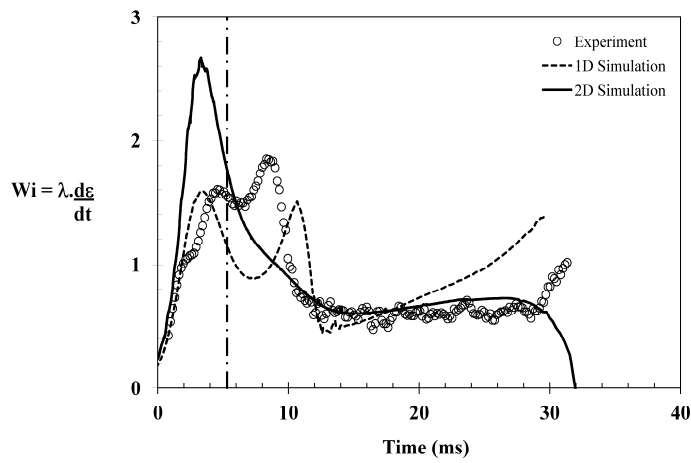**5.3ms**　　　　**18.5ms**　　　　**25.3ms**　　　　**38.5ms**

873

874 **Figure 18:** Comparison between the experimental transient profiles for the

875 DEP+5wt%PS110 and the simulations of (a) the 1D and (b) the 2D cases using the

876 FENE-CR multimode constitutive equations.

877
878

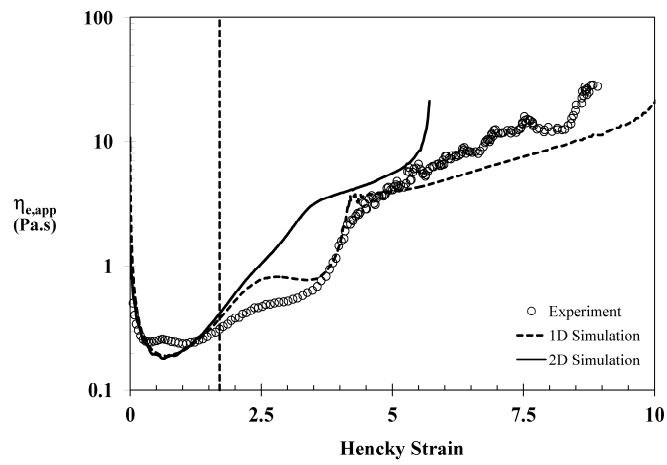$$Wi = \lambda . \frac{d\varepsilon}{dt}$$

879

880

881 **Figure 19**: Evolution of the Weissenberg number as a function of the Hencky strain.

882 Transient Weissenberg numbers were calculated using $\lambda = 3.2$ms for experimental

883 data, $\lambda = 2.89$ms and $\lambda = 5.1$ms for 1D simulation and 2D simulation data using multi

884 modes FENE-CR as constitutive equation.

885

886

Figure 20: Evolution of the transient apparent extensional viscosity $\eta_{e,app}$ as a function of the Hencky strain ε for computed from the mid filament evolution shown in Fig. 12.

890

891